Research Square

Preprints are preliminary reports that have not undergone peer review.
They should not be considered conclusive, used to inform clinical practice,
or referenced by the media as validated information.

Spin-Matched Hydrogenation via High-Spin Co^{2+} Sites for Robust pH-Universal Ammonia Electrosynthesis

Yang Liu

liuyang_fd@fudan.edu.cn

Fudan University https://orcid.org/0000-0001-5586-623X

Jiangnan Lv

Shanxi Normal University

Wanting Rong

Shanxi Normal University

Tingting Liang

Shanxi Normal University

Tong Zhang

Fudan University

Yuxin Zhang

Shanxi Normal University

Qiqi Dai

Shanxi Normal University

Yizhi Gao

Shanxi Normal University

Lanfang Wang

Shanxi Normal University

Article

Keywords:

Posted Date: September 7th, 2026

DOI: https://doi.org/10.21203/rs.3.rs-10919228/v1

License: This work is licensed under a Creative Commons Attribution 4.0 International License.
Read Full License

Additional Declarations: There is **NO** Competing Interest.

Abstract

Electrocatalytic nitrate reduction reaction (NO_3^-RR) offers a sustainable route for NO_3^- remediation and ammonia (NH_3) electrosynthesis, yet selective NH_3 formation is frequently limited by the sluggish hydrogenation of deeply reduced nitrogen intermediates, particularly under neutral conditions. Herein, inverse-spinel $CoFe_2O_4$ containing high-spin octahedral (O_h)-Co^{2+} centers is developed as a spin-defined electrocatalyst for pH-universal NO_3^-RR. The high-spin O_h-Co^{2+} centers enable spin-matched interaction with the singly occupied N 2p-derived frontier orbital of open-shell *NH, thereby promoting spin-allowed electron transfer and lowering the key *NH → *NH_2 hydrogenation barrier. In neutral electrolyte, $CoFe_2O_4$ delivers an NH_3 Faradaic efficiency (FE) of 95.1% at − 0.9 V_{RHE} and a remarkable NH_3 yield rate of 2.2 mmol h^{-1} cm^{-2} at − 1.0 V_{RHE}, ranking among the best reported neutral NO_3^-RR electrocatalysts. It maintains high NH_3 selectivity and durability in acidic and alkaline media, with NH_3 FEs exceeding 90% over a broad alkaline potential window and stable operation for over 200 h. In situ characterization reveals attenuated *NH accumulation and accelerated downstream hydrogenation, consistent with the proposed spin-matched pathway. These findings identify late-stage *NH hydrogenation as a spin-sensitive kinetic bottleneck and establish metal–adsorbate spin matching as a design principle for pH-universal NO_3^-RR.

Introduction

The imbalance in the global nitrogen cycle has become an increasingly severe environmental challenge.[1] Excessive nitrogen fertilizer use and industrial activities have caused persistent nitrate (NO_3^-) accumulation in surface and groundwater, leading to eutrophication and threats to ecosystems and human health.[2,3] Meanwhile, ammonia (NH_3), a key feedstock for fertilizer production and a promising carbon-free energy carrier, is conventionally synthesized via the Haber-Bosch process under high-temperature and high-pressure conditions.[4,5] However, this process consumes approximately 2% of the global energy supply and contributes about 1.4% of global carbon dioxide emissions.[6,7] Electrocatalytic nitrate reduction reaction (NO_3^-RR) offers a sustainable route for simultaneous NO_3^- remediation and NH_3 synthesis under ambient conditions.[8–10] Nevertheless, NO_3^-RR is a multistep proton-coupled electron transfer process involving the sequential reduction of NO_3^- to NO_2^- and NO_2^- to NH_3, thereby exhibiting inherently sluggish kinetics.[11] Particularly, in neutral NO_3^-RR systems, NH_3 formation critically depends on the continuous supply of active hydrogen (*H) species and the efficient stepwise hydrogenation of nitrogen-containing intermediates.[12,13] The kinetic imbalance between these two processes can lead to the accumulation of reaction intermediates, thereby markedly decreasing the activity and selectivity of neutral NO_3^-RR. Therefore, developing catalysts that can ensure sufficient *H supply while selectively accelerating key intermediate hydrogenation is crucial for selective NO_3^--to-NH_3 conversion.

In recent years, strategies such as single-atom doping,[14] alloying,[15] and interfacial engineering have been widely adopted to modulate the electronic structure and local reaction environment of catalysts, thereby enhancing their reactivity and product selectivity.[16,17] However, NO_3^-RR involves consecutive deoxygenation and hydrogenation steps, with different intermediates exhibiting distinct electronic structures and spin characteristics. These conventional strategies predominantly rely on structural or compositional modifications to indirectly improve catalytic performance, which limits their ability to precisely regulate intermediate evolution and product selectivity. In contrast, spin regulation can directly influence orbital occupation, electron transfer, and metal-intermediate coupling, providing a more direct and fundamental route for controlling reaction pathways and product selectivity.[18] Previous studies have shown that spin effects are critical to NO_3^-RR. For example, Sun *et al.* constructed adjacent Cu – Co sites by introducing Cu into a high-entropy oxide, which increased the local spin moment of the Co centers and enhanced the Cu – Co synergistic interaction and NH_3 production performance, demonstrating that heterometal incorporation can effectively regulate the spin configuration of catalysts.[19] Subsequently, Dai and coworkers induced spin polarization at Fe – Ti dual sites through oxygen-vacancy engineering. The unpaired Fe and Ti 3d electrons interacted with key reaction intermediates, thereby facilitating $*NO_3$ deoxygenation and accelerating *NO hydrogenation.[20] However, most existing studies have primarily focused on overall spin polarization or early-stage $*NO_x$ activation, while how spin coupling between metal active centers and adsorbates governs the late-stage hydrogenation kinetics of deeply deoxygenated nitrogen intermediates remains insufficiently understood. In particular, the conversion of *NH to $*NH_2$ involves not only coupled proton-electron transfer but also the concerted reorganization of the metal – N bond, N 2p frontier-orbital occupation, and the local spin configuration. Therefore, although a continuous supply of *H is necessary for deep hydrogenation, it does not necessarily ensure that *NH can be further hydrogenated along a low-energy reaction pathway. Spin matching describes a configuration in which the frontier states of a metal active site and an adsorbed intermediate both contain unpaired electrons and are energetically aligned, spatially compatible, and spin-allowed, thereby promoting metal–adsorbate orbital hybridization and electron transfer. By contrast, incompatible spin configurations or mismatched orbital energies and symmetries weaken orbital coupling and increase the energetic cost of electron transfer and bond reorganization.[21] Therefore, constructing well-defined metal active sites capable of forming spin-matched coupling with *NH represents a promising strategy for regulating the spin-dependent kinetics of this critical late-stage hydrogenation step. In this context, spinel $CoFe_2O_4$ provides a suitable model platform because its characteristic cation distribution and well-defined octahedral (O_h) Co coordination environment enable direct investigation of the spin-dependent coupling between Co centers and nitrogen-containing intermediates.[22] Guided by these considerations, we propose that O_h-Co^{2+} sites can enable spin-matched O_h-Co^{2+}–*NH coupling to promote key *NH hydrogenation during NO_3^-RR. Beyond neutral conditions, achieving pH-universal NO_3^-RR is also crucial for practical NO_3^- remediation and NH_3 synthesis, as real NO_3^--containing wastewater often spans a broad pH range. Therefore, developing intrinsically spin-regulated catalysts

that maintain high activity, selectivity, and stability across diverse pH conditions is highly desirable for broadly applicable NO_3^--to-NH_3 conversion.

To validate this design concept, we synthesized spinel $CoFe_2O_4$ with intrinsic high-spin O_h-Co^{2+} sites as a pH-universal NO_3^-RR electrocatalyst. The optimized $CoFe_2O_4$ catalyst achieves a remarkable NH_3 yield rate of 2.2 mmol h^{-1} cm^{-2} with an outstanding Faradaic efficiency (FE) of 95.1%, surpassing most reported electrocatalysts and ranking among the top-performing systems for neutral NO_3^-RR. Moreover, $CoFe_2O_4$ maintains high activity, selectivity, and stability under acidic and alkaline conditions, demonstrating its broad pH adaptability. Mechanistic investigations reveal a site-specific O_h-Co^{2+}–*NH spin-matched hydrogenation mechanism, in which spin-matched O_h-Co^{2+}–*NH coupling facilitates the key *NH → *NH_2 hydrogenation step and thereby accelerates the deep reduction of NO_3^- to NH_3. This work establishes site-specific metal–intermediate spin matching as a powerful strategy for regulating key hydrogenation steps and provides a mechanistic foundation for the rational design of efficient, selective, and durable pH-universal NO_3^-RR electrocatalysts.

Results and Discussion

$CoFe_2O_4$ adopts a typical inverse spinel structure, denoted as $[Fe^{3+}]_{Td}[Co^{2+}Fe^{3+}]_{Oh}O_4$, where Fe^{3+} ions are distributed at both T_d and O_h sites and Co^{2+} ions mainly occupy O_h sites.[23,24] This well-defined cation distribution gives rise to octahedrally coordinated Co^{2+} centers with an open-shell d^7 electronic configuration, providing a suitable model platform for investigating spin-dependent coupling between Co centers and the deeply deoxygenated NH intermediate. Accordingly, spinel-structured Co_3O_4 and Fe_3O_4 were selected as reference materials with distinct cation distributions, coordination geometries, and electronic configurations. Co_3O_4 adopts a conventional spinel structure, with Co^{2+} ions occupying the T_d sites and Co^{3+} ions residing at the O_h sites. In contrast, Fe_3O_4 adopts an inverse spinel structure, with Fe^{2+} preferentially occupying O_h sites and Fe^{3+} distributed across both T_d and O_h sites (Supplementary Fig. 1).[25–27] The total density of states (TDOS) further shows that $CoFe_2O_4$ exhibits a higher density of electronic states near the Fermi level than Co_3O_4 and Fe_3O_4, suggesting greater electronic-state availability for interfacial charge transfer during NO_3^-RR (Supplementary Fig. 2).[28] Therefore, $CoFe_2O_4$ serves as an ideal model catalyst for investigating the O_h-Co^{2+}–*NH spin-matched hydrogenation mechanism (Fig. 1a).

We next examined the electronic origin of O_h-Co^{2+}–*NH coupling from the perspectives of crystal-field configuration and spin-resolved frontier-orbital interactions. In $CoFe_2O_4$, O_h-Co^{2+} exhibits a high-spin d^7 electronic configuration with a $t_{2g}^5 e_g^2$ occupancy, giving rise to singly occupied e_g-derived states near the Fermi level. When these Co 3d states are energetically aligned, spatially symmetry-compatible, and spin-allowed with the singly occupied N 2p-derived frontier state of NH, effective spin-matched Co 3d – N

2p coupling can occur. Such coupling enhances metal–adsorbate orbital hybridization and facilitates the electronic and bonding reorganization associated with *NH hydrogenation. In contrast, O_h-Co^{3+} in Co_3O_4 generally adopts a low-spin closed-shell $t_{2g}^6 e_g^0$ configuration, and therefore does not provide the same singly occupied e_g derived frontier state for coupling with *NH (Fig. 1b). These electronic-structure differences provide a basis for examining how site-specific spin compatibility influences the *NH-to-$*NH_2$ conversion.

To validate the proposed O_h-Co^{2+}–*NH spin-matched hydrogenation mechanism, we calculated the Gibbs free energy profiles of NO_3^-RR over $CoFe_2O_4$, Co_3O_4, and Fe_3O_4 under neutral conditions. As shown in Fig. 1c, all three catalysts follow a stepwise NO_3^- adsorption, deoxygenation, and hydrogenation pathway toward NH_3 formation. Notably, $CoFe_2O_4$ exhibits a more favorable reaction free energy for the *NH → $*NH_2$ conversion than Co_3O_4 and Fe_3O_4, indicating that its local electronic environment thermodynamically facilitates this late-stage hydrogenation step. This trend is consistent with the proposed spin-compatible interaction between the O_h-Co^{2+} 3d states and the N 2p-derived frontier state of *NH. After confirming the favorable *NH hydrogenation of $CoFe_2O_4$ under neutral conditions, we further calculated the Gibbs free energy profiles under acidic and alkaline conditions to evaluate the pH adaptability of the proposed mechanism (Supplementary Tables 1 and 2). As depicted in Fig. 1d, the key *NH → $*NH_2$ hydrogenation step on $CoFe_2O_4$ is thermodynamically spontaneous under both acidic and alkaline conditions. Under acidic conditions, abundant proton supply facilitates the successive hydrogenation process of nitrogen-containing intermediates. Under alkaline conditions, although reactive *H species are mainly generated through H_2O dissociation and proton transfer, $CoFe_2O_4$ still enables a feasible NO_3^--to-NH_3 conversion pathway (Supplementary Figs. 3 – 5). These results indicate that the O_h-Co^{2+}–*NH spin-matched hydrogenation mechanism remains effective across pH-variable environments, thereby providing theoretical support for the pH-universal NO_3^-RR performance of $CoFe_2O_4$.

In addition to the Co-centered *NH hydrogenation step, we further analyzed the partial density of states (PDOS) of NO_3^- adsorbed at different reaction sites and quantitatively evaluated the electronic-state overlap. The PDOS reveals pronounced Fe 3d – O 2p overlap between the Fe sites in $CoFe_2O_4$ and adsorbed NO_3^-, suggesting that Fe – O orbital hybridization contributes to NO_3^- adsorption and N – O bond activation (Supplementary Fig. 6). In neutral media, proton supply represents another critical bottleneck after NO_3^- activation, because the low availability of free protons makes *H species mainly originate from H_2O dissociation. Therefore, O – H bond cleavage and subsequent proton transfer are essential for sustaining intermediate hydrogenation in neutral media.[29] To probe this process, we systematically evaluated the H_2O dissociation capabilities of different catalytic sites. The dissociation energy of H_2O on the low-spin O_h-Co^{3+} site of Co_3O_4 is − 1.12 eV. In sharp contrast, the high-spin O_h-Co^{2+} site of $CoFe_2O_4$ exhibits a much more negative H_2O dissociation energy of − 2.84 eV, indicating a

thermodynamically more favorable O − H bond cleavage process (Fig. 1e). Additional calculations show that the H_2O dissociation energies at the Fe_3O_4 surface and the Fe site of $CoFe_2O_4$ are − 2.21 and − 2.26 eV, respectively (Supplementary Figs. 7 and 8). Notably, the high-spin O_h-Co^{2+} site in $CoFe_2O_4$ shows the most favorable H_2O dissociation energetics among these sites, suggesting its superior capability for continuously generating reactive *H species. This efficient *H supply can sustain the subsequent hydrogenation of nitrogen-containing intermediates, especially the key *NH-to-*NH_2 conversion, thereby supporting the O_h-Co^{2+}–*NH spin-matched hydrogenation pathway.

To experimentally validate the proposed O_h-Co^{2+}–*NH spin-matched hydrogenation mechanism, $CoFe_2O_4$ was synthesized via a hydrothermal route using metal nitrates as precursors, followed by alkaline precipitation, hydrothermal treatment, and subsequent calcination.[30] For comparison, Co_3O_4 and Fe_3O_4 were prepared using literature-established synthetic routes, with their structural and morphological characterizations shown in the Supporting Information (Supplementary Figs. 9 and 10).[31,32] As shown in Fig. 2a, the X-ray diffraction (XRD) pattern shows that the characteristic peaks at 30.1°, 35.4°, 43.1°, 57.0°, and 62.6° can be indexed to the (220), (311), (400), (511), and (440) planes of $CoFe_2O_4$ (PDF#01-083-3445), respectively, confirming the formation of the $CoFe_2O_4$ catalyst. Transmission electron microscopy (TEM) images reveal a nanospherical morphology of $CoFe_2O_4$, with a particle size distribution of 13 − 14 nm (Fig. 2b; Supplementary Fig. 11), while high-resolution TEM (HRTEM) images display that the exposed (220) crystal plane has a lattice spacing of 0.29 nm, which agrees well with the XRD results (Fig. 2c). Aberration-corrected scanning TEM (AC-STEM) further reveals an ordered atomic arrangement with an interatomic spacing of 3.4 Å within the $CoFe_2O_4$ lattice (Fig. 2d). Meanwhile, HAADF-STEM and corresponding energy dispersive X-ray spectroscopy (EDS) elemental mapping reveals a homogeneous distribution of Fe, Co, and O throughout the superlattice (Fig. 2e). The M − H curves further reveal the distinct magnetic differences among the oxide catalysts. $CoFe_2O_4$ exhibits the highest magnetization under an external magnetic field, whereas Fe_3O_4 shows a relatively weaker magnetic response and Co_3O_4 displays almost no obvious hysteresis behavior. The pronounced magnetic response of $CoFe_2O_4$ is consistent with its intrinsic high-spin characteristics and provides experimental support for the proposed spin-related catalytic mechanism (Fig. 2f). Collectively, these results confirm the successful synthesis of phase-pure $CoFe_2O_4$ nanospheres with a uniform morphology and pronounced spin-related magnetic characteristics.

The surface chemical states and coordination environments of $CoFe_2O_4$ were investigated using X-ray photoelectron spectroscopy (XPS) and X-ray absorption fine structure (XAFS) spectroscopy. The Fe 2p XPS spectrum displays two pairs of peaks characteristic of Fe^{3+}. The peaks at 710.1/723.4 eV and 713.0/725.8 eV are attributed to Fe^{3+} located at O_h and T_d sites, respectively (Fig. 3a).[33] Meanwhile, the Co 2p spectra are observed at binding energies of 779.4 and 782.0 eV, which are associated with Co^{2+} species mainly occupying O_h sites in the inverse spinel framework. Additionally, the pronounced shake-up satellite features observed in the Co 2p XPS spectra arise from strong multiplet splitting and ligand-

to-metal charge-transfer excitations characteristic of high-spin Co^{2+}. The satellite located at approximately 6 eV higher binding energy relative to the Co $2p_{3/2}$ main peak serves as a fingerprint of high-spin Co^{2+}, indicating that Co in $CoFe_2O_4$ predominantly adopts a high-spin Co^{2+} configuration and preferentially occupies O_h site (Fig. 3b).[19,34,35] The O 1s spectrum shows a main peak at 529.6 eV, assigned to metal-oxygen bonding, and a shoulder at 531.2 eV, which is ascribed to oxygen vacancies (Fig. 3c).[36] The energy threshold of the Fe K-edge for $CoFe_2O_4$ is higher than that of Fe foil and close to those of Fe_2O_3 (Fe^{3+}) and Fe_3O_4 ($Fe^{2+/3+}$). The Co K-edge absorption threshold of $CoFe_2O_4$ lies below those of Co_2O_3 (Co^{3+}) and Co_3O_4 ($Co^{2+/3+}$) but above that of Co foil (Figs. 3d and 3g). The Fourier-transform (FT) spectra of the Fe K-edge XAFS for $CoFe_2O_4$, elucidating the local atomic structure around the Fe centers. The FT-EXAFS spectra reveal dominant features at 1.4 and 2.6 Å, which correspond to the nearest-neighbor Fe − O and Fe(O_h) − M(O_h) bond distances in $CoFe_2O_4$, the symbol “M” refers to the cations (either Fe or Co), respectively (Fig. 3e; Supplementary Fig. 12 and Supplementary Table 3).[33] The FT-EXAFS spectra reveal dominant features at 1.5 and 2.6 Å, which correspond to the nearest-neighbor Co − O and Co(O_h) − M(O_h) bond distances in $CoFe_2O_4$ (Fig. 3h; Supplementary Fig. 13 and Supplementary Table 4). The wavelet transform (WT) contour plots further show maximum intensities for Fe(O_h) − M(O_h) and Co(O_h) − M(O_h) scattering at k values of 5.8 and 5.7 $Å^{-1}$, respectively, consistent with the typical local coordination structure of $CoFe_2O_4$ (Figs. 3f and 3i). These XPS and XAFS results collectively verify the Fe^{3+}/Co^{2+} electronic states and inverse-spinel coordination structure of $CoFe_2O_4$, providing experimental evidence for intrinsic high-spin O_h-Co^{2+} centers that underpin the proposed O_h-Co^{2+}–*NH spin-matched hydrogenation mechanism.

Considering that neutral media more closely resemble practical NO_3^--containing wastewater environments, we first evaluated the NO_3^-RR performance of the $CoFe_2O_4$ catalyst in a three-electrode system using an H-type cell in neutral electrolyte. All potentials were calibrated against the reversible hydrogen electrode (RHE). The concentrations of NO_3^-, NO_2^-, NH_3 and H_2 were subsequently quantified by UV − vis spectrophotometry and gas chromatography, respectively (Supplementary Figs. 14 − 17).[37,38] Linear sweep voltammetry (LSV) curves were first recorded to evaluate the activity of the $CoFe_2O_4$ and reference samples in sulfate electrolyte with and without KNO_3. The $CoFe_2O_4$ catalyst delivers the highest current density at the same potential, which can be attributed to its lower charge-transfer resistance compared with Co_3O_4 and Fe_3O_4 (Fig. 4a; Supplementary Fig. 18). Subsequently, potentiostatic electrolysis was conducted to quantitatively evaluate the electrocatalytic NO_3^-RR performance of three catalysts (Supplementary Fig. 19). As shown in Fig. 4b, $CoFe_2O_4$ catalyst maintains a high NH_3 FE across a wide potential window, the optimal NO_3^-RR performance at − 0.9 V_{RHE} with an NH_3 FE of 95.1% and a remarkable NH_3 yield rate of 2.2 mmol h^{-1} cm^{-2} at − 1.0 V_{RHE}. This performance significantly outperforms that of most reported neutral NO_3^-RR systems (Fig. 4d; Supplementary Table 5).[12,39–49] Furthermore, the NO_3^-RR performances of $CoFe_2O_4$, Co_3O_4 and Fe_3O_4 were

systematically compared under identical conditions. $CoFe_2O_4$ exhibits markedly higher NH_3 FE and yield rate than Co_3O_4 and Fe_3O_4, confirming its superior catalytic activity toward NO_3^-RR. In comparison, Co_3O_4 delivers an NH_3 FE of 74.6%, while Fe_3O_4 shows a lower NH_3 FE of 62.4% (Fig. 4c; Supplementary Fig. 20). Further analysis of NO_2^- selectivity reveals that Fe_3O_4 favors the initial reduction of NO_3^- to NO_2^- but the subsequent hydrogenation steps are kinetically hindered, leading to NO_2^- accumulation rather than efficient conversion to NH_3 (Supplementary Fig. 21). These results further demonstrate that $CoFe_2O_4$ not only promotes NO_3^- activation but, more importantly, facilitates the downstream hydrogenation of nitrogenous intermediates, consistent with the proposed O_h-Co^{2+}–*NH spin-matched hydrogenation mechanism. Using the World Health Organization (WHO) guideline value for NO_3^- in drinking water as a benchmark, we further assessed the NO_3^- removal capability of $CoFe_2O_4$ by monitoring the time-dependent concentrations of NO_3^- and N-containing products during electrolysis. The NO_3^- concentration decreased continuously with the concomitant accumulation of NH_3 and fell below the WHO guideline value within 4 h (Fig. 4e).[50] Meanwhile, the selectivity toward NH_4^+–N reached ~ 99%, confirming the efficient removal of NO_3^- and its highly selective conversion into NH_4^+–N. Taken together, these results experimentally confirm that the superior neutral NO_3^-RR performance of $CoFe_2O_4$ originates primarily from the O_h-Co^{2+}–*NH spin-matched hydrogenation mechanism, which accelerates downstream intermediate hydrogenation toward NH_3.

To verify the origin of the produced NH_3 and ensure the accuracy of the colorimetric quantification, we further performed a series of control experiments. Isotopically labeled $^{15}NO_3^-$/$^{14}NO_3^-$ was used separately as nitrogen sources, and the electrolysis products were analyzed by ^{1}H nuclear magnetic resonance (^{1}H NMR), with maleic acid used as an external standard (Supplementary Fig. 22).[51] After electrolysis at − 0.9 V_{RHE}, the ^{1}H NMR spectra of the $^{15}NO_3^-$ and $^{14}NO_3^-$ electrolytes displayed characteristic doublet and triplet signals, respectively.[52] These results unambiguously confirm that the NH_3 is originated from the NO_3^-RR process, rather than atmospheric contaminants. The concentration of generated NH_3 was further quantified by ^{1}H NMR. The NH_3 FEs determined by ^{1}H NMR were consistent with the values obtained using the colorimetric method (Supplementary Fig. 23). Moreover, negligible NH_3 was detected when the reaction was performed in 0.5 M sulfate electrolyte, further confirming that the produced NH_3 originates from NO_3^-RR (Supplementary Fig. 24).

To systematically evaluate the electrocatalytic performance of the $CoFe_2O_4$ catalyst for continuous NH_3 synthesis, a series of 40 consecutive electrocatalytic cycling tests were conducted. Even after 40 cycles, the $CoFe_2O_4$ catalyst maintained an exceptional NH_3 FE and NH_3 yield (Fig. 4f). Subsequently, we assembled a two-electrode membrane electrode assembly (MEA) device employing $CoFe_2O_4$ as the cathode and Pt mesh as the anode. The $CoFe_2O_4$ catalyst maintains a high current density of approximately − 400 mA cm^{-2} at − 2.3 V, with a FE for NH_3 exceeding 80% and a stable NH_3 production

rate of nearly 2.0 mmol h^{-1} cm^{-2} over 200 hours (Fig. 4g). Overall, these results demonstrate that $CoFe_2O_4$ achieves a favorable balance of activity, selectivity, and stability for electrocatalytic NH_3 synthesis under neutral conditions.

To assess the pH adaptability of $CoFe_2O_4$ beyond neutral conditions, we further evaluated its NO_3^-RR performance in both acidic and alkaline electrolytes. In acidic electrolyte (0.05 M H_2SO_4 with 0.2 M KNO_3, pH = 1.8), $CoFe_2O_4$ exhibited a pronounced cathodic reduction current, indicating effective NO_3^- activation and reduction (Fig. 5a). At − 1.3 V_{RHE}, the catalyst achieved a maximum NH_3 yield rate of 1.05 mmol h^{-1} cm^{-2}, with an NH_3 FE of 91.62%. Similarly, under alkaline conditions (1 M KOH with 0.2 M KNO_3, pH = 13.8), the catalyst also showed a significant reduction current response (Fig. 5c). Notably, the catalyst maintained NH_3 FEs exceeding 90% over a broad potential window from − 0.2 to − 0.5 V_{RHE}, reaching a maximum NH_3 yield rate of 6.3 mmol h^{-1} cm^{-2} at − 0.5 V_{RHE} (Figs. 5b and 5d). Long-term stability tests further showed that, after 200 h of continuous electrolysis, the NH_3 FE exhibited negligible decay under both acidic and alkaline conditions, confirming the excellent durability of $CoFe_2O_4$ in different pH media (Figs. 5e and 5f). Together with its outstanding neutral NO_3^-RR performance, these results demonstrate the robust pH-universal adaptability of $CoFe_2O_4$. Moreover, comparison with previously reported NO_3^-RR catalysts in acidic and alkaline electrolytes shows that $CoFe_2O_4$ delivers competitive NH_3 yield rates, particularly in alkaline media, highlighting its excellent broad-pH adaptability and promising practical potential (Fig. 5g; Supplementary Table 6).

The intrinsic high-spin state in $CoFe_2O_4$ stabilizes the spinel coordination framework during catalytic cycling, thereby endowing the catalyst with enhanced structural stability and durability. To assess the structural stability of $CoFe_2O_4$ during NO_3^-RR, we first monitored its crystal-structure evolution using potential-dependent XRD. As shown in Fig. 6a, the positions and intensities of the main diffraction peaks of $CoFe_2O_4$ remain essentially unchanged over the potential range from − 0.6 to − 1.0 V_{RHE}, indicating that the spinel phase is well preserved during electrolysis. Furthermore, in situ XAFS was employed to track the electronic structures and local coordination environments of the Fe and Co sites in $CoFe_2O_4$ under reaction conditions. As the potential was shifted from open-circuit potential (OCP) to − 1.0 V_{RHE}, no obvious absorption-edge shifts were observed in either the Fe K-edge or Co K-edge XANES spectra. The absorption-edge positions remained within the range defined by the corresponding + 2/+3 valence, indicating that the Fe/Co sites in $CoFe_2O_4$ are largely stable during NO_3^-RR without significant valence reconstruction or irreversible redox changes (Figs. 6b and 6c). Meanwhile, the positions and intensities of the Fe − O, Fe(O_h) − M(O_h), Co − O, and Co(O_h) − M(O_h) coordination peaks in the Fe and Co K-edge FT-EXAFS spectra show no significant variation, further demonstrating that the local spinel coordination framework of $CoFe_2O_4$ is well maintained under working potentials (Figs. 6d and 6e). In addition, post-electrolysis TEM, XRD, and XPS characterizations reveal no obvious changes in the morphology, crystal structure, or surface chemical states of the catalyst, further confirming the robustness of $CoFe_2O_4$ under

NO_3^-RR conditions (Supplementary Fig. 25). Taken together, these results demonstrate that the intrinsic high-spin spinel framework of $CoFe_2O_4$ exhibits excellent structural and electronic stability during NO_3^-RR, providing a stable active-site foundation for sustained *NH hydrogenation over high-spin O_h-Co^{2+} sites.

We further combined in situ Raman, in situ Fourier-transform infrared spectroscopy (FTIR), Electron paramagnetic resonance (EPR) spin-trapping, and differential electrochemical mass spectrometry (DEMS) measurements to track the dynamic evolution of *H species and nitrogen-containing intermediates during NO_3^-RR. In situ Raman spectra show that, over $CoFe_2O_4$, the NO_3^- symmetric stretching vibration at 1046 cm^{-1}. and the NH_4^+-related vibration at 1197 cm^{-1} emerge as the potential shifts negatively from OCP to − 1.1 V_{RHE}, whereas no pronounced accumulation of *NH intermediates is detected (Fig. 6f).[47,53] In contrast, pronounced *NH-related Raman signals appear over both Co_3O_4 and Fe_3O_4, with a characteristic peak at 1583 cm^{-1}.[53] Fe_3O_4 also shows a *NO_2-related signal at 1351 cm^{-1}, suggesting that nitrogen-containing intermediates are more readily accumulated on the reference catalysts, whereas $CoFe_2O_4$ facilitates their subsequent conversion (Figs. 6g and 6h).[54] These results indicate that $CoFe_2O_4$ more effectively promotes the successive hydrogenation of nitrogen-containing intermediates, thereby suppressing surface accumulation of *NH. In situ FTIR further reveals the stepwise evolution of NO_3^-RR intermediates on $CoFe_2O_4$. As the potential shifts negatively, several absorption bands associated with NO_3^- reduction and subsequent hydrogenation appear, including *NH_4 at 1459 cm^{-1}, *NH at 1311 cm^{-1}, *NO_2 at 1232 cm^{-1}, *NH_2 at 1154 cm^{-1}, and *NO_3 at 1057 cm^{-1} (Fig. 6i).[53,55,56] The emergence and enhancement of these signals indicate that NO_3^- undergoes stepwise deoxygenation and successive hydrogenation on the $CoFe_2O_4$ surface. In particular, the enhanced *NH-related signals further confirm that $CoFe_2O_4$ favors the deep hydrogenation of downstream intermediates toward NH_3 formation. EPR spin-trapping measurements show that the 5,5-dimethyl-1-pyrroline N-oxide (DMPO) − H signal over $CoFe_2O_4$ is much weaker than those over Fe_3O_4 and Co_3O_4, indicating that *H species generated on $CoFe_2O_4$ are rapidly consumed in the successive hydrogenation of NO_3^--derived intermediates rather than accumulating on the surface (Fig. 6j).[57] Moreover, DEMS detects gas signals corresponding to NO, N, NH, NH_2, and NH_3, further supporting a NO_3^- to NH_3 pathway involving stepwise deoxygenation and successive hydrogenation (Fig. 6k).[58] Overall, these in situ characterization results demonstrate that $CoFe_2O_4$ efficiently couples H_2O-dissociation-derived reactive *H species with the successive hydrogenation of downstream nitrogen-containing intermediates. In particular, the absence of obvious *NH accumulation over $CoFe_2O_4$, together with the formation of NH_4^+, *NH_2, and * NH_3-related signals, indicates that high-spin O_h-Co^{2+} sites effectively promote the key *NH → *NH_2 hydrogenation step. These findings provide strong experimental evidence for the proposed O_h-Co^{2+}–*NH spin-matched hydrogenation mechanism.

Conclusion

In summary, we developed inverse-spinel $CoFe_2O_4$ with intrinsic high-spin O_h-Co^{2+} centers as an efficient and durable electrocatalyst for pH-universal NO_3^-RR. Theoretical analyses reveal that the partially occupied e_g-derived frontier states of O_h-Co^{2+} enable spin-matched coupling with the N 2p-derived frontier orbital of *NH, thereby promoting the key *NH → *NH_2 hydrogenation step. $CoFe_2O_4$ delivers outstanding neutral NO_3^-RR performance with an NH_3 FE of 95.1% at − 0.9 V_{RHE} and an NH_3 production rate of 2.2 mmol h^{-1} cm^{-2} at − 1.0 V_{RHE}, while maintaining high selectivity and durability under acidic and alkaline conditions. Mechanistic investigations further demonstrate that $CoFe_2O_4$ preserves its spinel framework during NO_3^-RR, while efficiently coupling H_2O-dissociation-derived *H supply with downstream nitrogen-intermediate hydrogenation. In situ characterizations reveal suppressed *NH accumulation and accelerated *NH-to-*NH_2 conversion over $CoFe_2O_4$, providing experimental evidence for the O_h-Co^{2+}–*NH spin-matched hydrogenation mechanism. This work establishes the O_h-Co^{2+}–*NH spin-matched hydrogenation mechanism for accelerating late-stage intermediate hydrogenation in NO_3^-RR, providing a spin-state design principle for robust electrocatalysts toward sustainable NH_3 synthesis and NO_3^- remediation.

Methods

Materials

Iron(III) nitrate nonahydrate (99.99%), Cobaltous nitrate hexahydrate (99%), ferric Chloride hexahydrate (99.9%), Cetyltrimethylammonium bromide (98%), thiourea (99%), ferrous chloride tetrahydrate (99.5%), ammonia solution (25 wt %), Sodium carbonate (99.5%), hydrochloric acid (36–38%), Ethyl alcohol (≥ 99.5%), Nafion perfluorinated resin solution (5 wt%), potassium hydroxide (90%), maleic acid (≥ 99%), sodium citrate tribasic hydrate (≥ 99%), sodium nitroferricyanide(Ⅲ) dihydrate (≥ 99%), salicylic acid(≥ 99%), sodium hypochlorite (4.00-4.99wt%), N-(1-Naphthyl)-ethylenediamine dihydrochloride (≥ 98%), potassium nitrate (≥ 99%), ammonium chloride (99.5%), sodium hydroxide (≥ 98%), potassium nitrite (97%), sulfanilamide (98%), dimethyl sulfoxide-d6 (99.9%) were purchased from Sigma-Aldrich. Potassium nitrate-15N (≥ 99%), ammonium chloride-^{15}N, were purchased from Aladdin. Carbon paper was purchased from Toray Industries. All chemicals were used as received without further purification.

Synthesis of catalysts

Synthesis of $CoFe_2O_4$. $CoFe_2O_4$ was synthesized via a co-precipitation–hydrothermal route.[59] $Co(NO_3)_2{\cdot}6H_2O$ (0.03 M) and $Fe(NO_3)_3{\cdot}9H_2O$ (0.06 M) were dissolved in 75 mL of deionized water, followed by dropwise addition of 5 mol·L^{-1} NaOH at 60°C to adjust the pH to 11. The resulting

precipitate was subjected to hydrothermal treatment at 150°C for 24 h, then washed, dried at 80°C, and calcined at 400°C for 3 h to obtain $CoFe_2O_4$.

Synthesis of Fe_3O_4. Under a nitrogen atmosphere, $FeCl_2·4H_2O$ (7.5 mmol) and $FeCl_3·6H_2O$ (15 mmol) were dissolved in 60 mL of 0.24 mol·L^{-1} HCl solution to suppress iron hydrolysis. Subsequently, 50 mL of 10 wt% $NH_3·H_2O$ solution was added, and the mixture was heated at 90°C for 1 h to form Fe_3O_4 precipitates. A $Na_3Cit·2H_2O$ solution ($m(Na_3Cit·2H_2O)/m(Fe_3O_4)$ = 10%) was then introduced as a dispersant, and the reaction was further maintained at 90°C for an additional 1 h. After completion, the system was cooled to room temperature under nitrogen protection. The resulting black precipitate was collected and repeatedly washed with deionized water and ethanol to obtain Fe_3O_4 nanodispersions.[32]

Synthesis of Co_3O_4. $Co(NO_3)_2·6H_2O$ (0.4 mol) and Na_2CO_3 (0.5 mol) were separately dissolved in deionized water and then mixed, followed by stirring in a 50°C water bath for 2 h to form a precipitate. The resulting precipitate was washed, dried overnight at 80°C, and subsequently calcined at 550°C for 4 h with a heating rate of 1°C min^{-1} to obtain the Co_3O_4 catalyst.[31]

Characterization.

Powder X-ray diffraction (XRD) measurements were performed on a Rigaku Ultima IV diffractometer using a Cu Kα radiation source. Samples were prepared by drop-casting concentrated NC dispersions onto customized glass slides. Transmission electron microscopy (TEM) and high-resolution TEM (HRTEM) images were acquired on a JEOL JEM 2100 operated at 200 kV. Energy-dispersive X-ray spectroscopy (EDS) elemental mapping was conducted using an Ultim Max 80 detector. TEM specimens were prepared by depositing dilute NC dispersions onto carbon-coated gold grids and drying under ambient conditions. X-ray photoelectron spectroscopy (XPS) measurements were carried out on a Thermo Fisher Scientific K-Alpha spectrometer equipped with an Al Kα source (1486.6 eV, spot size 400 μm), with the chamber pressure maintained below 4×10^{-9} mbar. X-ray absorption fine structure (XAFS) spectra were collected in transmission (or fluorescence) mode on a Rapid XAFS 2M system (Anhui Absorption Spectroscopy Analysis Instrument Co., Ltd.) at 20 kV and 20 mA. Raman spectra were recorded on a Renishaw InVia Raman microscope using a 532 nm excitation laser. Ultraviolet–visible (UV – vis) absorption spectra were obtained using a HITACHI UH5700 UV–visible – NIR spectrophotometer. Nuclear magnetic resonance (^{1}H NMR) spectra were recorded at 600 MHz on a Bruker BioSpin spectrometer. Electrochemical online differential electrochemical mass spectrometry (DEMS) measurements were performed using a QAS100-D mass spectrometer in a customized electrochemical cell equipped with an Ag/AgCl reference electrode and a Pt mesh counter electrode. The pH values of electrolytes were measured using a PHS-3E pH meter (Leici). The macroscopic magnetic properties were characterized using a Physical Property Measurement System (PPMS, Quantum Design).

DFT calculations.

All the DFT calculations were performed using the Vienna *Ab initio* Simulation Package (VASP).[60,61] The exchange-correlation interactions were described by the Perdew-Burke-Ernzerhof (PBE) functional within the generalized gradient approximation (GGA).[62] The projector augmented wave (PAW) method was employed to treat the electron-ion interactions.[63] A plane-wave energy cutoff of 450 eV was used, and the Brillouin zone was sampled with a 3 × 3 × 1 Monkhorst–Pack k-point grid.

Spin polarization was incorporated in all calculations to properly account for magnetic effects, with the initial magnetic moments assigned as 4 μ_B for Fe atoms and 3 μ_B for Co atoms. The convergence thresholds for the self-consistent field (SCF) calculations were set to 10^{-5} eV for energy and 0.02 eV $Å^{-1}$ for atomic forces. The DFT + U approach was applied to better describe the localized d-electron states, with U − J values of 3.5 eV for Co and 4.0 eV for Fe. Van der Waals interactions were treated using the DFT-D3 dispersion correction scheme.[64] The calculated structures and charge distributions were visualized using the VESTA software package.[65]

The Gibbs free energy changes (ΔG) were calculated using the following formula:

$$\Delta G = \Delta E + \Delta ZPE - T\Delta S$$

where ΔE is the difference of electron energies calculated by DFT; ΔZPE and ΔS are the changes of zero-point energy and entropy, respectively, which are obtained from vibrational frequencies. T is the temperature (298.15 K).

Electrochemical measurements.

Electrochemical measurements were carried out at room temperature using a CHI 760E electrochemical workstation in a three-electrode H-type cell separated by a Nafion 117 membrane. Prior to assembly, the Nafion membrane was pretreated by sequential immersion in 5% H_2O_2, ultrapure water, 5% H_2SO_4, and ultrapure water, with each step maintained at 80°C for 1 h. Both the cathodic and anodic compartments were filled with 30 mL of electrolyte containing 0.5 M Na_2SO_4 and 0.2 M KNO_3. An Ar flow (20 sccm) was maintained throughout the electrochemical measurements. The catalyst ink was prepared by dispersing 10 mg of catalyst powder in a solvent mixture of 950 µL ethanol and 50 µL Nafion solution, followed by homogenization and ultrasonication for 30 min to obtain a uniform suspension. A defined volume of the ink was then drop-cast onto a 1 × 1 cm^2 carbon paper substrate, achieving a catalyst loading of 1 mg cm^{-2}. An Ag/AgCl electrode was used as the reference electrode, and a 2 × 2 cm^2 Pt sheet served as the counter electrode. The potentials recorded versus Ag/AgCl were converted to the reversible hydrogen electrode (RHE) scale using the relationship:

$$E_{RHE} = E_{Ag/AgCl} + 0.197\ V + 0.0591 \times pH$$

Cyclic voltammetry (CV) scans were performed to activate the cathodes. Typically, 50 CV cycles were conducted in an electrolyte containing 0.5 M Na_2SO_4 and 0.2 M KNO_3 over a potential range of − 0.6 to −

1.0 V_{RHE} at a scan rate of 100 $mV{\cdot}s^{-1}$. Linear sweep voltammetry (LSV) measurements were recorded at a scan rate of $mV{\cdot}s^{-1}$. An 80% iR compensation was applied during all electrochemical measurements. Potentiostatic tests were conducted at the designated applied potentials under ambient conditions for 0.5 h.

MEA stability test. The membrane electrode assembly (MEA) stability tests were conducted using a customized MEA electrolyzer. The MEA consisted of a $CoFe_2O_4$ cathode, a Nafion 117 proton exchange membrane, and a Pt sheet anode. The catholyte and anolyte reservoirs each contained 2.0 L of electrolyte, which was circulated at a flow rate of 20 mL min^{-1}. during operation.

Electrochemical in situ ATR-FTIR tests. Electrochemical in situ ATR-FTIR measurements were conducted on a Thermo Nicolet iS50 spectrometer equipped with liquid nitrogen-cooled MCT detector and the VeeMAX III ATR accessory (Pike Technologies) with a single bounce silicon crystal covered with an Au membrane in internal reflection mode. A custom-built spectroelectrochemical cell (Gaossunion) was used, with the anode and cathode compartments separated by a Nafion 117 membrane. The measurements were conducted in electrolyte containing 0.5 M Na_2SO_4 and 0.2 M KNO_3. The electrolyte was degassed by bubbling Ar gas for 30 min before the measurement. The All spectra were recorded at 4 cm^{-1} resolution by averaging 32 scans. Typically, a background spectrum was first acquired and then a range of cathodic potentials (OCP to − 1.1 V_{RHE}, with 0.1 V interval) were applied using a potentiostat.

Products analysis

NO_3^- quantification. In a typical measurement, 0.2 mL of 1.0 M HCl and 0.02 mL of 0.8 wt.% sulphamic acid were introduced into the previously diluted solution. After thorough mixing, the absorbance was recorded using UV–vis spectrophotometry at wavelengths of 220 and 275 nm. The NO_3^- absorbance was determined according to the following equation: $A = A_{220nm} - 2A_{275nm}$.

NH_3 quantification. NH_3 concentrations were determined using the indophenol blue method with calibration curves established from standard NH_4Cl solutions (0 − 5.00 μg mL^{-1}). Electrolyte samples collected after NO_3^-RR at different potentials were diluted (10 − 200×) prior to analysis. For colorimetric detection, the diluted electrolyte was reacted with NaOH solution (1 M, containing 5.0 wt% salicylic acid and 5.0 wt% sodium citrate), NaClO (0.025 mL), and sodium nitroferricyanide (0.1 mL, 1.0 wt%). After incubation in the dark for 2 h, the absorbance was measured using a UV − vis spectrophotometer.

NH_3 quantification using ^1H NMR. Typically, the post-NO_3^-RR electrolyte was initially neutralized to pH 7.0 using a dilute H_2SO_4 solution. A mixture containing 4 mg maleic acid, 50 μL of 4 M H_2SO_4, and 50 μL $DMSO–d_6$ was introduced to 1 mL neutralized electrolyte prior to NMR tube transfer. A series of standard NH_4Cl solutions (0, 50, 100, 150, 200 and 300 ppm) to calibrate the concentration-peak area curve obtained from the NMR spectrum.

Determination and quantitation of NO_2^- using UV − vis. The color reagent was prepared by combining ultrapure water (50 mL), sulfanilamide (4 g), N-(1-naphthyl) ethylenediamine dihydrochloride (0.20 g), and phosphoric acid (10 mL, ρ = 1.70 g/mL). The electrolyte obtained from NO_3^-RR at different potentials was diluted 10 to 100 times to obtain a 5 mL solution before 0.1 mL color reagent was added. The absorption spectrum of the solution was measured using a UV − vis spectrometer after 20 min in dark.

Calculation of FE of all products.

$$FE_{NH3}=\frac{Q_{NH3}}{Q}=\frac{8Vc_{NH3}F}{Q}$$

$$FE_{NO_2^-}=\frac{Q_{NO_2^-}}{Q}=\frac{2Vc_{NO_2^-}F}{Q}$$

The flow rate of H_2 gas exiting the cathode compartment was monitored during electrolysis by using a mass flow meter (Sevenstar) to ensure a gas-tight setup. The cathode part was connected to a gas chromatograph (GC, 8860, Agilent) for quantification of gas products. Ar (99.999%) was used as the carrier gas. The amounts of H_2 were measured by using a flame ionization detector (FID). The Faradaic efficiency of H_2 was calculated as:

$$FE_{H_2}=\frac{Q_{H_2}}{Q}=\frac{2fVc_{H_2}PFt}{QRT}$$

where Q is the applied overall coulomb quantity (C), Q_{NH3}, Q_{NO2}^-, and Q_{H2} are the coulomb used for producing NH_3 and NO_2^-, respectively. V is the volume of the catholyte of the cathode chamber (30 ml), c_{NH3} and c_{NO2}^- are the concentration of NH_3 and NO_2^- generated, respectively. F is the Faraday constant (96485 C mol^{-1}), t is the reaction time (30 min), f (Ar gas flow rate) (20 sccm) during electrolysis, T (temperature) is 298.15 K, R (gas constant) is 8.314 atm·L/(mol·K), P (pressure) is 1 atm.

Data Availability

All data supporting the findings of this work are available in the Manuscript and Supplementary information. The source data generated in this study are provided in the Source Data file. Source data are provided with this paper. All data are available from the corresponding author upon request.

Declarations

Acknowledgements

This study was financially supported by the National Natural Science Foundation of China (52471224, 52301298, U24A2023 and 52431009). The authors would like to thank Fudan University Electron Microscopy Center for access of instrumentation.

Author Contributions

[#]J. Lv, W. Rong, and T. Liang. contributed equally to this work. The manuscript was written through contributions of all authors. All authors have given approval to the final version of the manuscript.

Competing Interests Statement

The authors declare no competing financial interest.

References

1. Wang Y et al (2025) Interfacial Water Structure Modulation on Unconventional Phase Non-Precious Metal Alloy Nanostructures for Efficient Nitrate Electroreduction to Ammonia in Neutral Media. Angew Chem Int Ed 64:e202508617
2. Wang K et al (2023) Intentional corrosion-induced reconstruction of defective NiFe layered double hydroxide boosts electrocatalytic nitrate reduction to ammonia. *Nat. Water* 1, 1068 – 1078
3. Liao W et al (2024) Sustainable conversion of alkaline nitrate to ammonia at activities greater than 2 A cm^{-2}. Nat Commun 15:1264
4. MacFarlane DR et al (2020) A Roadmap to the Ammonia Economy. *Joule* 4, 1186 – 1205
5. Li S et al (2022) ITO@TiO_2 nanoarray: An efficient and robust nitrite reduction reaction electrocatalyst toward NH_3 production under ambient conditions. *eScience* 2, 382 – 388
6. Suryanto BHR et al (2019) Challenges and prospects in the catalysis of electroreduction of nitrogen to ammonia. Nat Catal 2:290–296
7. Wang M et al (2021) Can sustainable ammonia synthesis pathways compete with fossil-fuel based Haber–Bosch processes? Energy Environ Sci 14:2535–2548
8. Dong Y, Li J, Yang X-Y (2022) Cu catalysts detour hydrogen evolution reaction. Matter 5:2537–2540
9. Lv J et al (2024) Engineering Nickel Dopants in Atomically Thin Molybdenum Disulfide for Highly Efficient Nitrate Reduction to Ammonia. Adv Funct Mater 34:2411491
10. Fu Y et al (2026) Copper–palladium hydride interfaces promote electrochemical ammonia synthesis. *Nat. Synth.* 5, 433 – 444
11. Wen W et al (2024) Modulating the Electrolyte Microenvironment in Electrical Double Layer for Boosting Electrocatalytic Nitrate Reduction to Ammonia. Angew Chem Int Ed 63:e202408382
12. Tahir W et al (2026) Covalent Organic Frameworks on Cu_2O Nanocubes as Rapid Proton/Electron Transfer Gates for Efficient NH_3 Electrosynthesis from Nitrate in Neutral Media. J Am Chem Soc 148:743–755

13. Yu J et al (2025) Influence of active hydrogen on pathway selection in electrochemical nitrate reduction. eScience 5:100350
14. Guo J et al (2026) Oxygen-Incorporation-Engineered Interfacial Water Modulation on Single-Atom Cu Sites for Enhanced Dilute Nitrate Electroreduction. Angew Chem Int Ed 65:e16401
15. Wang Y et al (2025) Interfacial Water Structure Modulation on Unconventional Phase Non-Precious Metal Alloy Nanostructures for Efficient Nitrate Electroreduction to Ammonia in Neutral Media. Angew Chem Int Ed Engl, e202508617
16. Li Z et al (2025) Stabilizing Cu^{0}-$Cu^{\delta+}$ sites via ohmic contact interface engineering for ampere-level nitrate electroreduction to ammonia. Nat Commun 16:8940
17. Huo M et al (2026) Synergistically Promoting Oxygen Electrocatalysis through the Precise Integration of Atomically-Dispersed Fe Sites and Co Nanoparticles. Adv Energy Mater 16:2405155
18. Lin L et al (2025) Advances in regulating the electron spin effect toward electrocatalysis applications. eScience 5:100264
19. Sun S et al (2024) Spin-related Cu-Co pair to increase electrochemical ammonia generation on high-entropy oxides. Nat Commun 15:260
20. Dai J et al (2024) Spin polarized Fe_1–Ti pairs for highly efficient electroreduction nitrate to ammonia. Nat Commun 15:88
21. Cao A, Nørskov JK (2023) Spin Effects in Chemisorption and Catalysis. *ACS Catal.* 13, 3456 – 3462
22. Zhao Q, Yan Z, Chen C, Chen J (2017) Spinels: Controlled Preparation, Oxygen Reduction/Evolution Reaction Application, and Beyond. Chem Rev 117:10121–10211
23. Dedi, Idayanti N, Kristiantoro T, Alam GFN, Sudrajat N (1964) Magnetic properties of cobalt ferrite synthesized by mechanical alloying. *AIP Conf. Proc.* (2018)
24. Orege JI et al (2023) Emerging spinel ferrite catalysts for driving CO_2 hydrogenation to high-value chemicals. Matter 6:1404–1434
25. Huo M et al (2025) Tailoring Octahedron-Tetrahedron Synergism in Spinel Catalysts for Acidic Water Electrolysis. J Am Chem Soc 147:10678–10689
26. Kaya S, Ogasawara H, Nilsson A (2015) Determination of the surface electronic structure of Fe_3O_4(111) by soft X-ray spectroscopy. Catal Today 240:184–189
27. Wang R-P et al (2022) Analyzing the Local Electronic Structure of Co_3O_4 Using 2p3d Resonant Inelastic X-ray Scattering. J Phys Chem C 126:8752–8759
28. Liang T et al (2025) Unveiling the Role of Topological Surface States in Boosting Electrocatalytic Nitrate Reduction to Ammonia. Adv Energy Mater 15:e03473
29. Hu Q et al (2025) Subnanometric Nickel Phosphide Heteroclusters with Highly Active $Ni^{\delta+}$–$P^{\delta-}$ Pairs for Nitrate Reduction toward Ammonia. J Am Chem Soc 147:12228–12238
30. Liu N et al (2023) Elucidating the structural evolution of highly efficient Co–Fe bimetallic catalysts for the hydrogenation of CO_2 into olefins. Appl Catal B 328:122476

31. Long Y et al (2025) Modulation of Co spin state at Co_3O_4 crystalline-amorphous interfaces for CO oxidation and N_2O decomposition. Nat Commun 16:1048
32. Sun Q et al (2023) Fe_3O_4 Nanodispersions as Efficient and Recoverable Magnetic Nanocatalysts for Sustainable PET Glycolysis. ACS Sustainable Chem Eng 11:7586–7595
33. Huang C-Y et al (2025) In Situ Identification of Spin Magnetic Effect on Oxygen Evolution Reaction Unveiled by X-ray Emission Spectroscopy. J Am Chem Soc 147:13286–13295
34. Brown DG, Weser U (1979) XPS Spectra of Spin-Triplet Cobalt(III) Complexes. Z für Naturforschung B 34:1468–1470
35. Zhou Z et al (2008) Electronic structure studies of the spinel $CoFe_2O_4$ by X-ray photoelectron spectroscopy. Appl Surf Sci 254:6972–6975
36. Sun J et al (2018) A Facile Strategy to Construct Amorphous Spinel-Based Electrocatalysts with Massive Oxygen Vacancies Using Ionic Liquid Dopant. Adv Energy Mater 8:1800980
37. Yuan Z-H et al (2025) Architecture Engineering and Phase Engineering of Rhodium Metallene Co-Boost Nitrite-to-Ammonia Electroconversion. Angew Chem Int Ed 64:e202509944
38. Xiong Y et al (2024) Regulating the Electrochemical Nitrate Reduction Performance with Controllable Distribution of Unconventional Phase Copper on Alloy Nanostructures. Adv Mater 36:2407889
39. Cheng X-F et al (2022) Coordination Symmetry Breaking of Single-Atom Catalysts for Robust and Efficient Nitrate Electroreduction to Ammonia. Adv Mater 34:2205767
40. Yang Y et al (2025) Self-Triggering a Locally Alkaline Microenvironment of Co_4Fe_6 for Highly Efficient Neutral Ammonia Electrosynthesis. J Am Chem Soc 147:8893–8905
41. Jin X et al (2026) Localized Active H* Enrichment by Cobalt Molecular Catalysts for Enhanced Electrocatalytic Nitrate Reduction. Angew Chem Int Ed, e24566
42. Wang Y et al (2025) Boosting Nitrate-to-Ammonia Conversion over Copper-Based Electrocatalysts by Facilitating Hydrogenation and Product Desorption. Angew Chem Int Ed 64:e202509090
43. Tian Q et al (2025) Nanocellular Organelle Engineering for Optimizing Reaction Microenvironments in Nitrate-to-Ammonia Electrocatalysis. Angew Chem Int Ed 64:e202516919
44. Zhu Y et al (2026) DFT-Guided Design and Synthesis of Bipyridine-Anchored Copper Single-Atom Catalysts for Efficient Nitrate-to-Ammonia Electroreduction Across a Broad pH Range. Angew Chem Int Ed Engl 65:e17715
45. Tian S et al (2025) Realizing Unconventional Tandem Nitrate Reduction for Efficient Ammonia Electrosynthesis Enabled by Co, Fe Dual-Site Conjugated Metal Organic Frameworks. Angew Chem Int Ed 64:e202510665
46. Hu Q et al (2025) Subnanometric Nickel Phosphide Heteroclusters with Highly Active $Ni^{\delta+}$-$P^{\delta-}$ Pairs for Nitrate Reduction toward Ammonia. J Am Chem Soc 147:12228–12238
47. Jia X et al (2026) Self-Sustaining Dynamic Alkaline Microenvironment-Mediated Efficient Nitrate Electroreduction to Ammonia on $MnFeO_x$ in Neutral Electrolyte. Angew Chem Int Ed 65:e4598330

48. Xu L et al (2026) Dynamic Cobalt Phase Transition Enables Self-Adaptive Electrocatalytic Nitrate-to-Ammonia Conversion in Neutral Media. Angew Chem Int Ed 65:e9755292
49. Chen B et al (2026) Boosting Cobalt Porphyrin for Selective Nitrate Electroreduction. Angew Chem Int Ed 65:e23415
50. Li M et al (2025) Fast Seawater Desalination Driven by Efficient Nitrate Reduction via Bimetallic Iron/Zinc Polyphthalocyanine Frameworks. Angew Chem Int Ed 64:e202506712
51. Zhang T et al (2024) Boosting Electrochemical Ammonia Synthesis via NO_x Reduction over Sulfur-Doped Copper Oxide Nanoneedle Arrays. Adv Energy Mater 14:2400790
52. Lv J et al (2025) Accelerating Nitrate Electroreduction to Ammonia via Metal–Support Interactions in Ni-WS_2 Catalysts. J Am Chem Soc 147:27708–27719
53. Li J et al (2025) Nanoflower-Like CuPd/CuO Heterostructure for an Energy-Output Electrocatalytic System Coupling Ammonia Electrosynthesis and Zinc-Nitrate Battery. Adv Funct Mater 35:2501527
54. Yu J et al (2025) Single Ag Atoms Induce Ag-N/O Bonds on WO_3 for Ultrastable Acid Ammonia Synthesis. Angew Chem Int Ed 64:e202507696
55. Peng C-K et al (2026) Spin-Selective Anti-Perovskite Enables Breakthrough Nitrate-to-Ammonia Electrocatalysis. Adv Mater 38:e23066
56. Meng L et al (2026) Steering the nitrate electroreduction pathway via nanoconfinement-induced hydrogen-bond network regulation. Nat Water 4:481–492
57. Lv J et al (2026) Spin-State Modulation of Nickel Enables High-Efficiency and Durable Nitrate Electroreduction to Ammonia. Adv Funct Mater 36:e75961
58. Xu H et al (2023) In Situ Confinement of Ultrasmall Metal Nanoparticles in Short Mesochannels for Durable Electrocatalytic Nitrate Reduction with High Efficiency and Selectivity. Adv Mater 35:2207522
59. Liu N et al (2023) Elucidating the structural evolution of highly efficient Co – Fe bimetallic catalysts for the hydrogenation of CO_2 into olefins. Appl Catal B 328:122476
60. Kresse G, Hafner J (1993) Ab initio molecular dynamics for liquid metals. *Phys. Rev. B* 47, 558 – 561
61. Kresse G, Hafner J (1994) Ab initio molecular-dynamics simulation of the liquid-metal-amorphous-semiconductor transition in germanium. *Physical review. B, Condensed matter* 49, 14251 – 14269
62. Perdew JP, Burke K, Ernzerhof M (1996) Generalized Gradient Approximation Made Simple [Phys. Rev. Lett. 77, 3865]. *Phys. Rev. Lett.* 78, 1396 – 1396 (1997)
63. Kresse G, Joubert D (1999) From ultrasoft pseudopotentials to the projector augmented-wave method. Phys Rev B 59:1758–1775
64. Grimme S, Antony J, Ehrlich S, Krieg H (2010) A consistent and accurate ab initio parametrization of density functional dispersion correction (DFT-D) for the 94 elements H-Pu. J Chem Phys 132:154104
65. Momma K, Izumi F (2011) VESTA 3 for three-dimensional visualization of crystal, volumetric and morphology data. J Appl Crystallogr 44:1272–1276

Figures

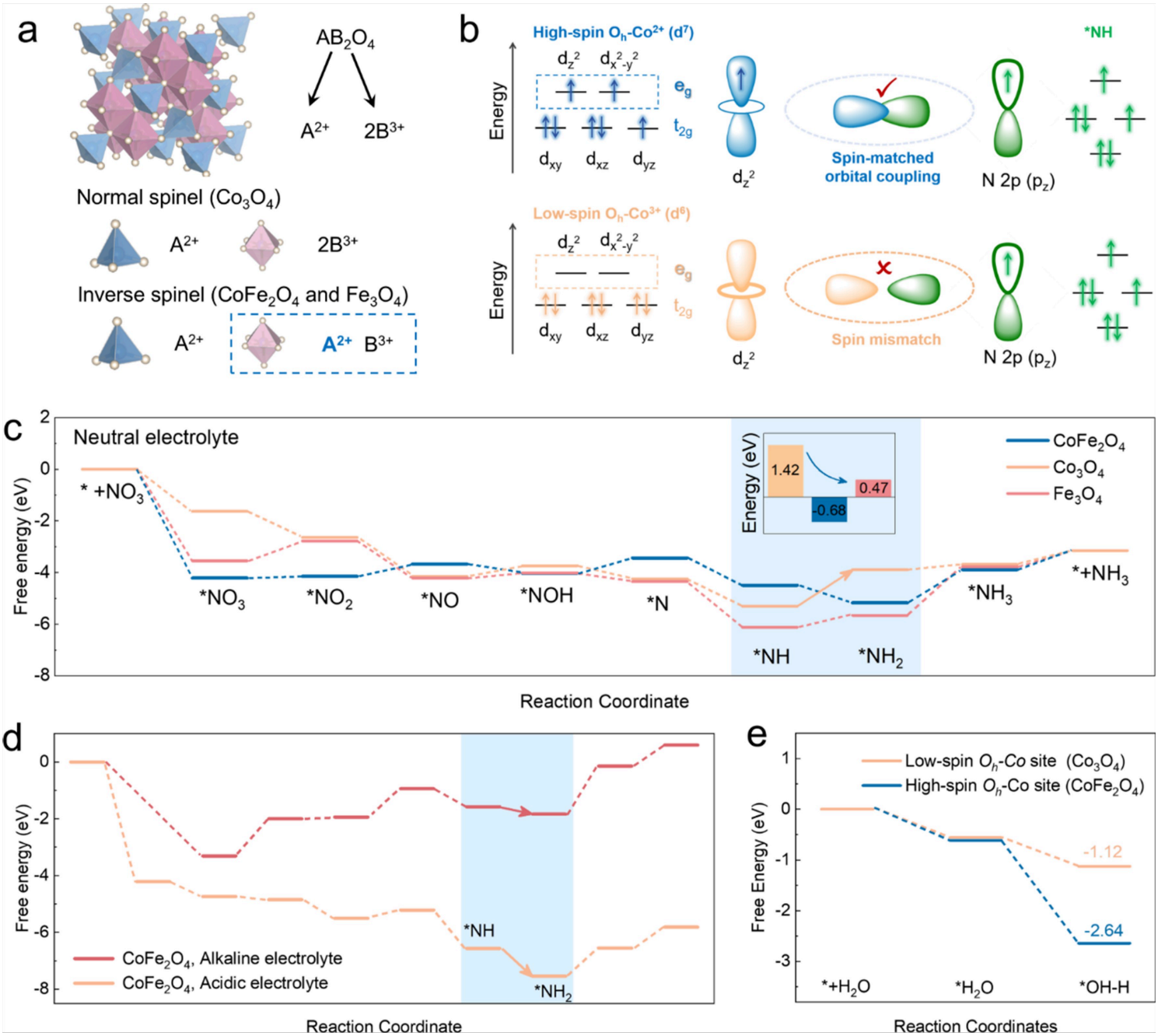


Figure 1

Structural configuration analysis and DFT calculations. (a) Structural configurations of normal and inverse spinel. (b) Schematic illustration of crystal-field splitting and spin-matched orbital coupling between high-spin O_h-Co^{2+} and adsorbed *NH. (c) Gibbs free-energy diagram of NO_3^-RR on $CoFe_2O_4$, Fe_3O_4, and Co_3O_4 under neutral conditions. (d) Gibbs free-energy diagram of NO_3^-RR on $CoFe_2O_4$ under acidic and alkaline conditions. (e) Free energy of H_2O dissociation on low-spin O_h-Co^{3+} sites in Co_3O_4 and high-spin O_h-Co^{2+} sites in $CoFe_2O_4$.

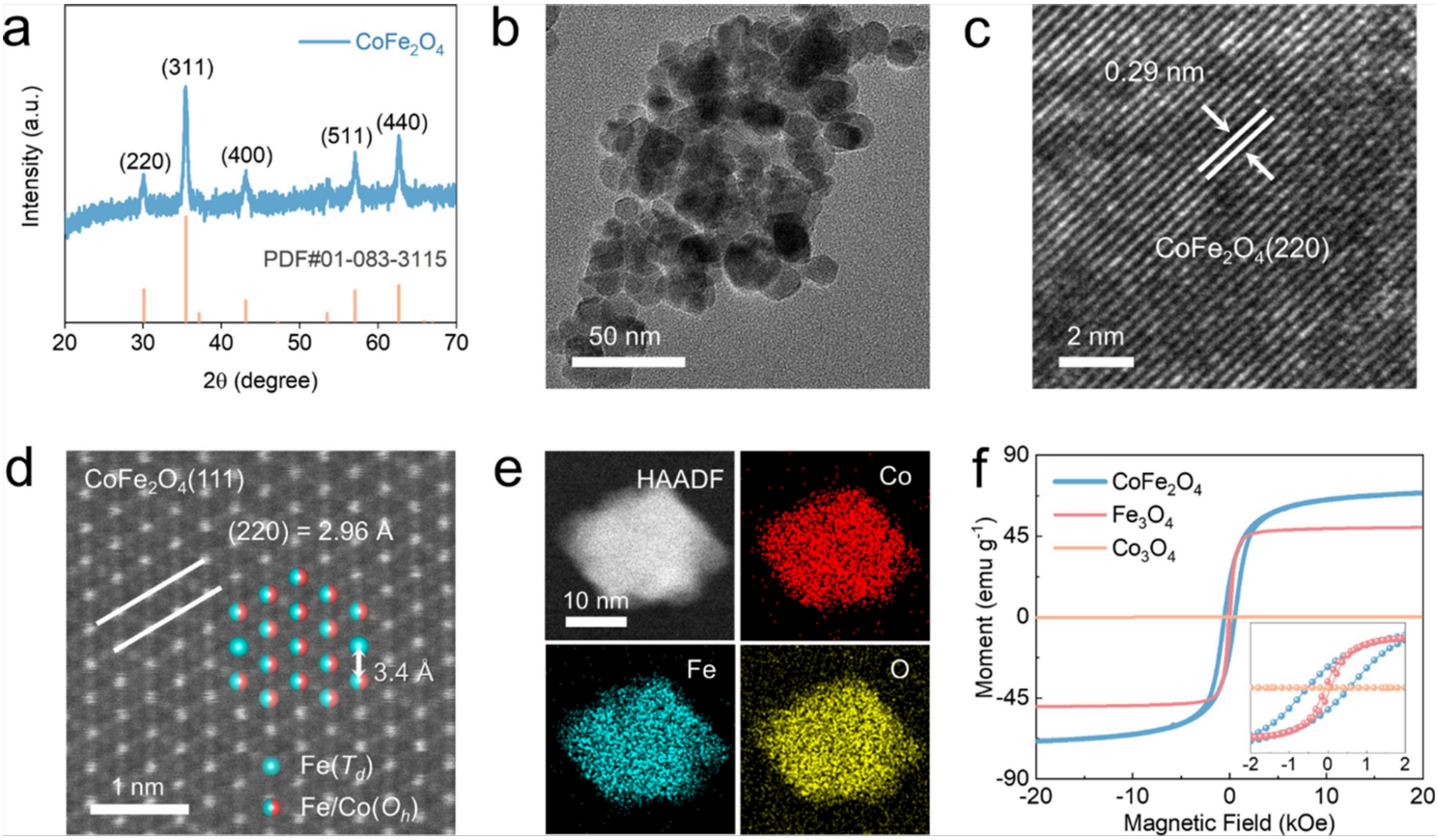


Figure 2

Structure and morphology of $CoFe_2O_4$. (a) XRD pattern. (b) TEM, c) HRTEM, and d) AC-STEM images of $CoFe_2O_4$ nanospheres. (e) EDS elemental maps of Co, Fe, and O of $CoFe_2O_4$ nanospheres. (f) Magnetic hysteresis loops of $CoFe_2O_4$, Fe_3O_4 and Co_3O_4.

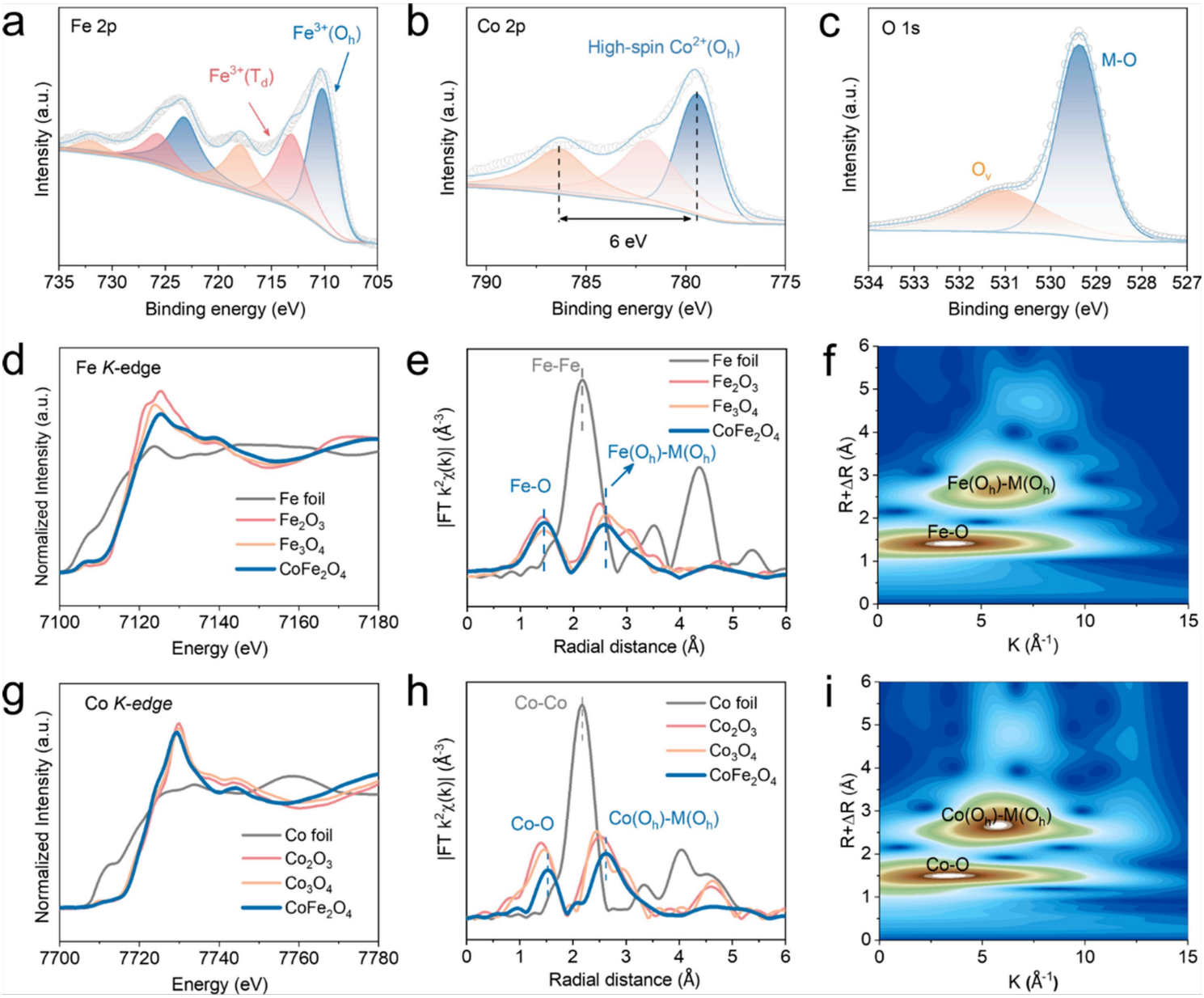


Figure 3

Surface chemical states and local coordination environments of $CoFe_2O_4$. XPS spectra of (a) Fe 2p, (b) Co 2p, and (c) O 1s regions of $CoFe_2O_4$. Normalized XAFS spectra at the (d) Fe K-edge and (g) Co K-edge. (e) Fe-edge XAFS spectra in the R space for Fe foil, Fe_2O_3, Fe_3O_4. (h) Co K-edge XAFS spectra in the R space for Co foil, Co_2O_3, Co_3O_4. WT-EXAFS contour plots at the (f) Fe K-edge and (i) Co K-edge of $CoFe_2O_4$.

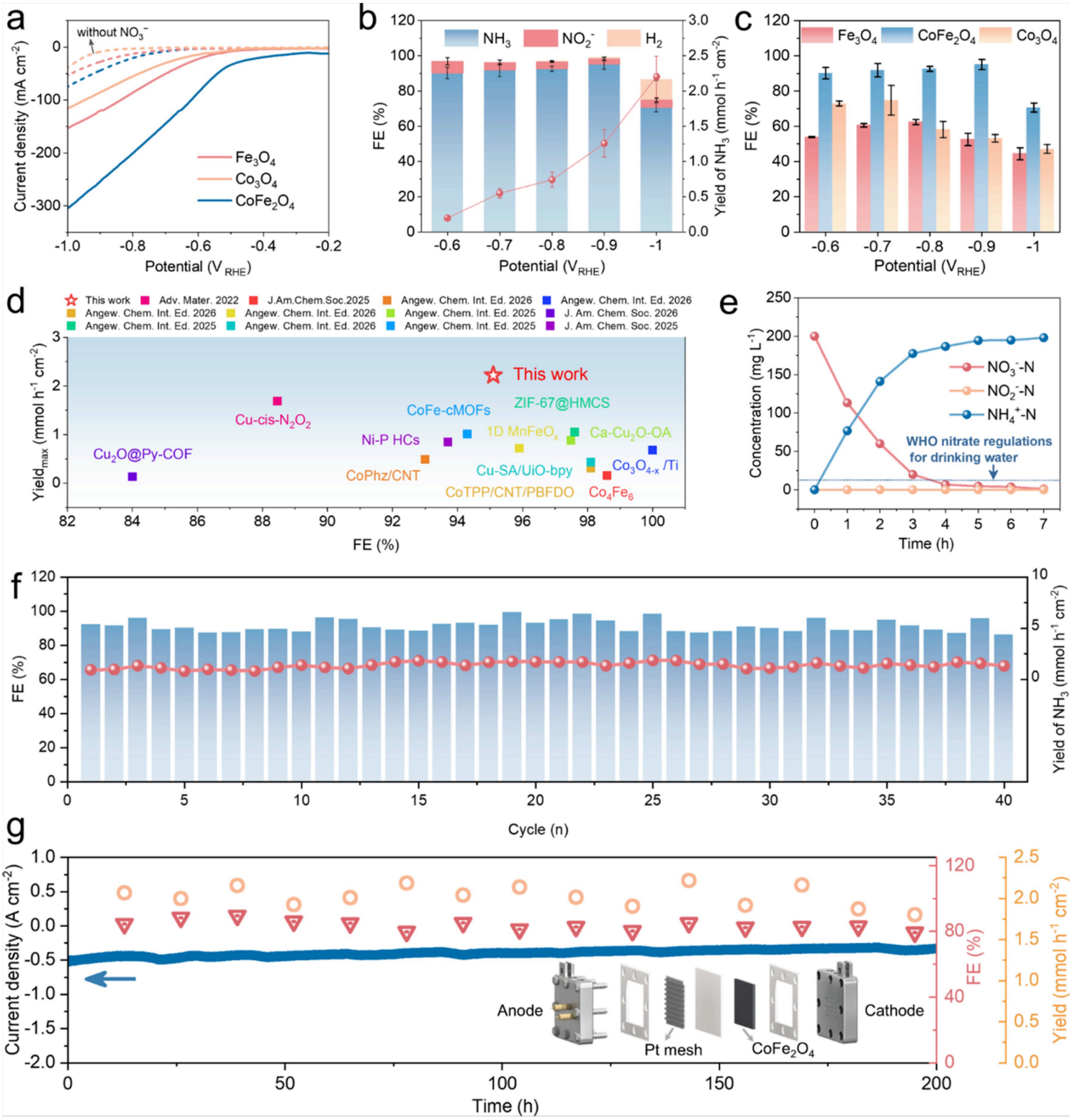


Figure 4

Electrochemical performance of NO_3^-RR in neutral electrolytes. (a) LSV curves of $CoFe_2O_4$, Fe_3O_4, and Co_3O_4 catalysts in sulfate electrolyte with and without KNO_3. (b) FE of NH_3, NO_2^-, and H_2 and NH_3 yield of $CoFe_2O_4$ at various applied potentials. (c) NH_3 FEs of the three catalysts tested at five potentials. (d) Comparison with some related catalysts. (e) Time-dependent concentration changes of NO_3^-–N, NH_4^+

−N, and NO_2^-−N by $CoFe_2O_4$ at −0.9 V_{RHE} in 0.5 M sulfate solution with initial concentration of 200 mg L^{-1} NO_3^-. (f) The consecutive 40 recycling test at −0.9 V_{RHE} over $CoFe_2O_4$. (g) Long-term electrocatalytic stability of the NO_3^-RR over $CoFe_2O_4$ at −2.3V using the MEA electrolyzer.

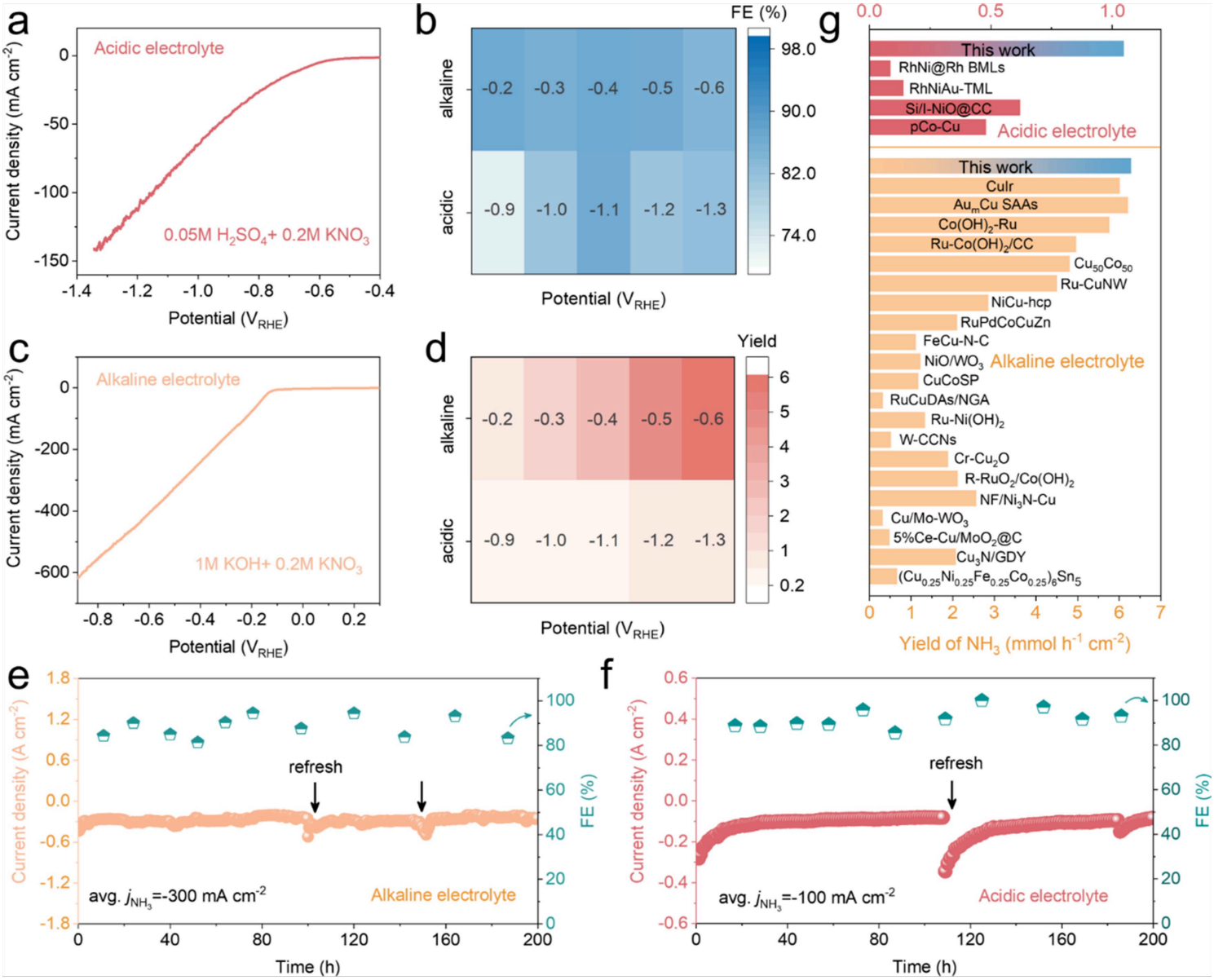


Figure 5

NO_3^-RR performance of $CoFe_2O_4$ in acidic and alkaline electrolytes. (a) LSV curve recorded in acidic electrolyte containing 0.05 M H_2SO_4 with 0.2 M KNO_3. (b) Heatmap of NH_3 FEs over different applied potentials in acidic and alkaline electrolytes. (c) LSV curve recorded in alkaline electrolyte containing 1.0 M KOH and 0.2 M KNO_3. (d) Heatmap of NH_3 yield rate over different applied potentials in acidic and alkaline electrolytes. Long-term electrolysis stability tests and corresponding NH_3 FEs in alkaline (e) and acidic (f) electrolytes. (g) Comparison of NH_3 yield rates between this work and recently reported NO_3^-RR catalysts in acidic and alkaline electrolytes.

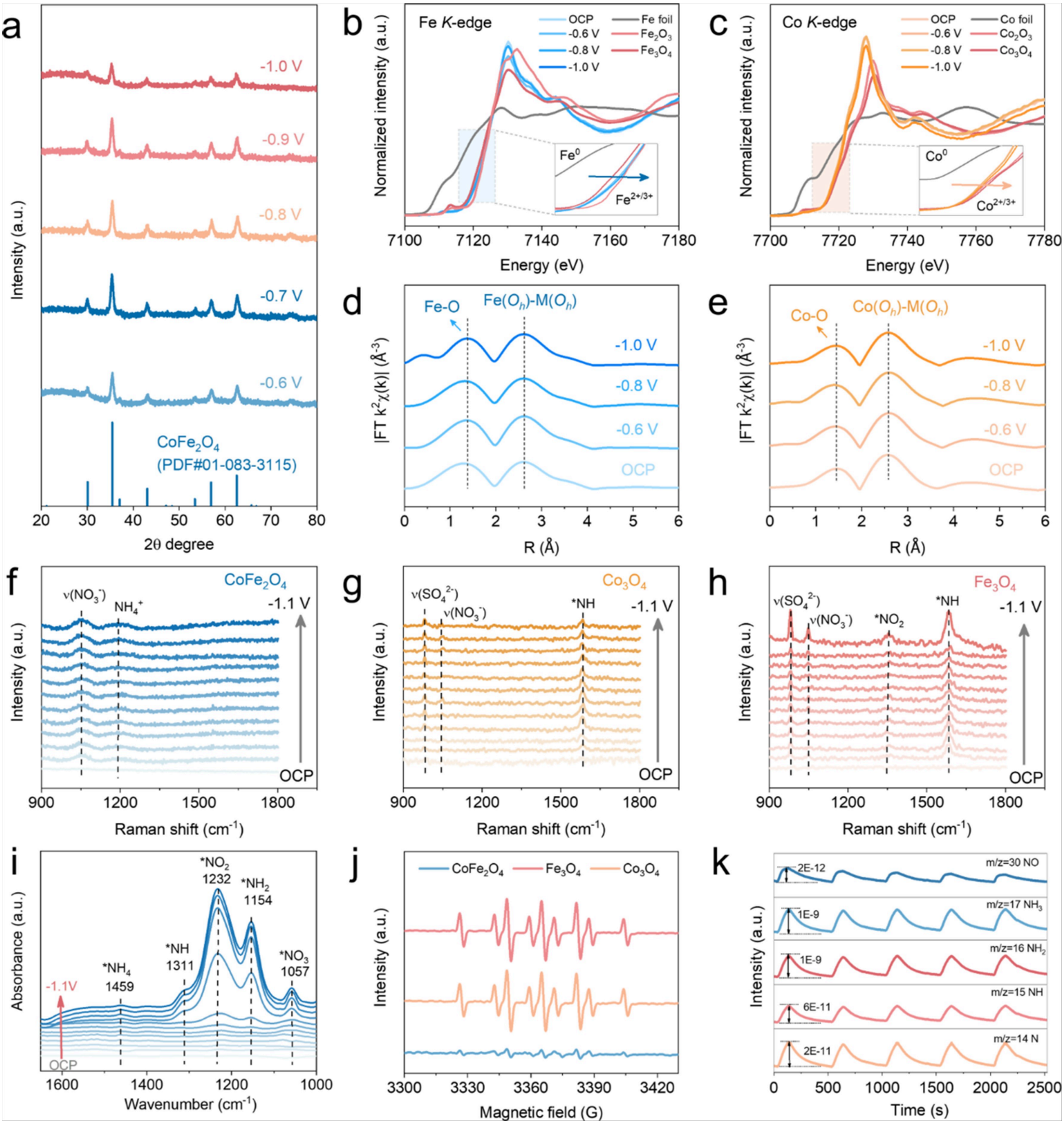


Figure 6

Mechanistic investigation of the NO_3^-RR over the $CoFe_2O_4$. (a) Potential-dependent XRD patterns of $CoFe_2O_4$. In situ XAFS spectra of (b) Fe K-edge and (c) Co K-edge of $CoFe_2O_4$. (d,e) Corresponding Fe K-edge and Co K-edge FT-EXAFS spectra. (f–h) In situ Raman spectra of $CoFe_2O_4$, Co_3O_4, and Fe_3O_4 during

NO_3^-RR. (i) In situ FTIR spectra of NO_3^-RR over $CoFe_2O_4$. (j) In situ EPR spectra of $CoFe_2O_4$, Co_3O_4, and Fe_3O_4 during NO_3^-RR. (k) In situ DEMS spectra of NO_3^-RR over $CoFe_2O_4$.

Supplementary Files

This is a list of supplementary files associated with this preprint. Click to download.

- Supportinginformation20260903.docx